Journal of Nuclear Materials 392 (2009) 292–300

Contents lists available at ScienceDirect

Journal of Nuclear Materials

journal homepage: www.elsevier.com/locate/jnucmat

Phase-field modeling of gas bubbles and thermal conductivity evolution in nuclear fuels

Shenyang Hu [a,*], Charles H. Henager Jr. [a], Howard L. Heinisch [a], Marius Stan [b], Michael I. Baskes [b], Steven M. Valone [b]

[a] Pacific Northwest National Laboratory, Richland, WA 99352, USA
[b] Los Alamos National Laboratory, Los Alamos, NM 87544, USA

A B S T R A C T

A phase-field model was developed to simulate the accumulation and transport of fission products and the evolution of gas bubble microstructures in nuclear fuels. The model takes into account the generation of gas atoms and vacancies, and the elastic interaction between diffusive species and defects as well as the inhomogeneity of elasticity and diffusivity. The simulations show that gas bubble nucleation is much easier at grain boundaries than inside grains due to the trapping of gas atoms and the high mobility of vacancies and gas atoms in grain boundaries. Helium bubble formation at unstable vacancy clusters generated by irradiation depends on the mobilities of the vacancies and He, and the continuing supply of vacancies and He. The formation volume of the vacancy and He has a strong effect on the gas bubble nucleation at dislocations. The effective thermal conductivity strongly depends on the bubble volume fraction, but weakly on the morphology of the bubbles.

Published by Elsevier B.V.

1. Introduction

Due to the creation of fission products and radiation damage, a complex microstructure evolution, such as the formation of gas bubbles, voids, precipitates and dislocation networks, occurs in nuclear fuels and cladding materials. These microstructural changes can result in fuel instability (such as fuel swelling, embrittlement, cracking and surface roughening) and thermodynamic property changes (such as phase instability, diffusivity and thermal conductivity). Therefore, understanding and predicting the microstructure evolution and its subsequent impact on material properties are crucial for scientific design of nuclear materials, optimizing fuel operation, and reducing uncertainty in operational and safety margins.

There has been extensive experimental investigation of the influence of fission products on properties and performance of nuclear fuels and cladding materials over the past 40 years [1–11]. Great progress has also been made in developing computational models for the prediction of gas release and fuel performance [12–22]. For example, the most advanced models include FASTGRASS [18], VICTORIA [19], MFPR [20,21] and FRAPCON [22]. These codes take into account a number of observed phenomena such as the production of fission gases, bubble nucleation, migration and coalescence, re-solution, temperature, temperature gradients, interlinked porosity and thermal conductivity. The codes are mainly based on two assumptions: (1) the evolution of the average concentrations of fission products follows kinetic rate equations; and (2) the growth kinetics of a single spherical gas bubble is described by the capillarity relationship. This relationship is valid only for the description of equilibrium crystals and generally fails under irradiation conditions when the fuel matrix is saturated with point defects. In addition, these models ignore or do not sufficiently take into account the effects of defects and defect structures, the morphology of bubbles, i.e., spatial and size distribution of bubbles, the elastic interaction among defects, bubbles and diffusive fission products and diffusivity inhomogeneity. All of these factors are important in determining both new phase nucleation and microstructure evolution kinetics, and hence, the microstructure and properties.

The phase-field method based on the fundamental thermodynamic and kinetic information has been emerging as a powerful computational approach at the mesoscale for predicting phase stability and microstructural evolution kinetics during many materials processes such as solidification, precipitation in alloys, ferroelectric domain evolution in ferroelectric materials, martensitic transformation, dislocation dynamics and electrochemical process [23–31]. This method describes a microstructure using a set of conserved and nonconserved variables that are continuous across the interfacial regions. The temporal and spatial evolution of the variables, i.e., the microstructural evolution, is governed by the Cahn-Hilliard nonlinear diffusion equation and the Alan Cahn relaxation equation. It uses input from thermodynamic and kinetic data from atomistic simulation, thermal dynamic calculations and

* Corresponding author. Tel.: +1 509 376 4432; fax: +1 509 376 0418.
E-mail address: Shenyang.hu@pnl.gov (S.Y. Hu).

0022-3115/$ - see front matter Published by Elsevier B.V.
doi:10.1016/j.jnucmat.2009.03.017

experiments, and outputs the kinetic information of microstructure evolution. Compared with atomistic simulation methods such as first principles methods and molecular dynamics [32,33], the phase-field method can deal with much larger length and time scales. Some kinetic Monte Carlo methods [34] might have time and length scales similar to the phase-field method. However, the phase-field method has the advantage of taking into account long-range interactions such as elastic interactions. If the calculation of energy differences requires evaluating the elastic solution at each MC step, then it will be a very time consuming simulation. Rate theory methods [14,21,35] have been used for simulating gas bubble evolution in metals and nuclear fuels. Although rate theories can deal with large time and length scales, it is difficult to include the effects of the morphology of gas bubbles, and the inhomogeneity of defect distributions and material properties on microstructure evolution with rate theory. It is very easy to integrate long-range interactions and the inhomogeneity of material properties into phase-field formulisms. These advantages give phase-field modeling the power to model the evolution of the microstructure and properties in the material at the mesoscale and linking atomistic and macroscopic simulations.

Microstructural evolution in irradiated materials is a complex process which involves extreme time and length scales ranging from individual atomic events such as point defect generation during radiation cascades on the scale of femtoseconds and nano-meters, to long term diffusion and macroscopic material property changes on the scale of years and meters. To study microstructural evolution requires not only accurate thermodynamic and kinetic properties of individual defects such as the generation rate of point defects, defect mobilities and their reactions, but also accurate thermodynamic and kinetic properties of the system such as chemical free energy and mechanical properties of different phases, interfacial energies, and interface mobility. In general, such information does not exist in a form that is readily used by such models. Therefore, this work develops and presents a qualitative phase-field model in order to demonstrate the ability to simulate microstructural evolution such as the accumulation of fission products and gas bubbles as well as internal stresses, and to study the effect of microstructures on thermal conductivity. All the results presented in this paper are qualitative because of both lack of accurate thermodynamic and kinetic properties and the simplifying assumptions used in the models. However, the work demonstrates the capability of the phase-field approach to provide important information such as the accumulation of fission products, three dimensional gas bubble morphology, the evolution of internal stresses and the effective thermal conductivity. With the development of accurate thermodynamic and kinetic data, and improvement of the model, quantitative results can be obtained in the future, which can be used as inputs for macro-scale fuel performance simulations such as FRAPCON.

2. Description of the phase-field model

The formation of gas bubbles is a direct consequence of the extremely low gas atom solubility in nuclear fuels and metals. However, the gas bubble nucleation and growth kinetics are strongly affected by a number of factors including the trapping of gas atoms by preexisting and evolving defects such as vacancies, dislocations and grain boundaries, mobility inhomogeneity as well as the generation rate of fission products. Fission products, depending on materials and nuclear reactions, will include typical inert gas atoms such as Kr, Xe and He, and lattice defects such as vacancies, vacancy clusters, dislocation loops, and interstitials. This work assumes that (1) all inert gas atoms are identical and mobile. The equation of state of the He gas phase is used to treat all gas bubbles as He bubbles to simplify the calculations and to reduce the number of different species; (2) a single vacancy is considered mobile, but vacancy clusters and dislocation loops are immobile; (3) the self-interstitial migration is very fast compared to vacancies, such that self-interstitials either recombine quickly with vacancies or become trapped by dislocations and grain boundaries so that they are not treated explicitly; and (4) the microstructure evolves through the diffusion of gas atoms and vacancies so that the gas phase and solid solution matrix phase are in equilibrium at all times. Although the system is dramatically simplified, all these assumptions can be resolved in the future by considering a multi-component system that is composed of different gas atoms and defects.

Describing the microstructure of a polycrystalline material with defects and diffusive species employs a number of continuous functions: $\varphi(\mathbf{r})$ to describe the polycrystalline grains and grain boundaries, $\eta_{ij}(\mathbf{r})$ the dislocation distributions, and $c_{gas}(\mathbf{r},t)$ and $c_{vac}(\mathbf{r},t)$ the concentrations of gas atoms and vacancies in the unit of atom/lattice site, respectively. $\mathbf{r}$ and t are spatial coordinates and time, respectively. The function $\varphi(\mathbf{r})$ is equal to 0 inside a grain, and varies smoothly from $0 \to 1 \to 0$ across a grain boundary. This work emphasizes the effect of free volume and diffusivity inhomogeneity in the grain boundaries on gas bubble formation and evolution while ignoring the anisotropy of grain boundaries. The function $\eta_{ij}(\mathbf{r})$ describes the discontinuous displacement across the slip plane in units of Burgers' vector b^{ij}. A detailed description of dislocations treated in this manner is given in Refs. [28,30].

In the phase-field framework, the total free energy of the system is written as a function of phase-field variables and includes the chemical free energy, gradient energy terms, and long-range interaction energy as:

$$E = \int_V (F(c_{gas}, c_{vac}) + \kappa_{gas}|\nabla c_{gas}|^2 + \kappa_{vac}|\nabla c_{vac}|^2 + F^{elastic}(\phi, \eta_{ij}, c_{gas}, c_{vac}))dV, \quad (1)$$

where $F(c_{gas}, c_{vac})$ is the chemical free energy, κ_{gas} and κ_{vac} are gradient coefficients associated with interfacial energy of gas bubbles, and the elastic energy $F^{elastic}$ is associated with the lattice mismatch of the defects.

2.1. Chemical free energy

Microstructural evolution in the phase-field model is driven by the minimization of the total free energy of the system described in Eq. (1). Generally speaking, a quantitative simulation relies on accurate chemical free energy and kinetic data. It is a big challenge to calculate the chemical free energy of fuel materials in terms of compositions and temperatures, especially when defects and irradiation-induced phases are considered. However, it is possible, in principle, to measure and calculate the thermodynamic equilibrium properties of each phase. These data can be used to construct a chemical free energy that provides the equilibrium thermodynamic properties of the system. However, we can treat the effect of chemical free energy on kinetics as an uncertainty and make a parametric investigation in the simulations. In this work, the system is assumed to be co-existence of a solid solution matrix phase and a gas phase at a given temperature. A model chemical free energy is constructed since no valid chemical free energy function exists. The chemical free energy tries to capture the following facts: (1) the very low solubility of vacancies and gas atoms in the matrix; (2) the strong binding of vacancies and gas atoms; and (3) in gas bubbles, the vacancy equilibrium concentration is $c_{vac}^{equ} = 1$ while gas atom equilibrium concentration is determined by the equation of state of the gas phase.

The chemical free energy has the form:

$$F(c_{gas}, c_{vac}) = f_{vac}(c_{vac}^4 + Ac_{vac}^3 + Bc_{vac}^2 + Cc_{vac} + D) + f_{gas}(c_{gas} - c_{gas}^0)^2 + E(c_{gas} - c_{gas}^0)(c_{vac} - c_{vac}^0), \quad (2)$$

where f_{gas}, f_{vac}, A, B, C, D and E are constants, and c_{gas}^0 and c_{vac}^0 is the solubility of gas atoms and vacancies in the matrix phase, respectively. E is associated with the binding energy between a vacancy and a gas atom. The terms f_{gas}, f_{vac}, A, B, C and D are determined by the equilibrium properties: equilibrium concentrations, common tangents, and gas bubble formation. The equation of state and chemical free energy of the He gas phase has been studied in Refs. [17,36,37]. A chemical free energy was constructed with the calculated equilibrium concentration of He gas at T = 1200 K. Fig. 1 shows the chemical free energy in terms of the concentration of He gas and vacancies in units of atom/lattice site. The parameters are listed in Table 1. Note that this chemical free energy only describes equilibrium properties. When the He concentration is zero a void phase and a solid solution matrix phase are in equilibrium. He gas phase becomes more stable than the void phase in the presence of He gas atoms. To develop a more accurate chemical free energy requires accurate thermodynamic data for the matrix and gas phases. As stated earlier, the objective of this work is to present the phase-field model and demonstrate it's capability. Future work will specifically study the effect of chemical free energies on microstructural evolution.

2.2. Elastic interaction energy

Experimental and theoretical studies demonstrate the great influence of defects generated under irradiation conditions on the bubble nucleation and growth [5,20]. Lattice mismatch around vacancies, gas atoms, dislocations and grain boundaries generates a stress field. The elastic interaction is one of the driving forces for migration of vacancies and gas atoms. The first step of bubble formation is the trapping of gas atoms and vacancies by defects. After reaching a certain filling state, n gas atoms plus vacancies complexes become stable against recombination with self-interstitial atoms. In the present work, the eigenstrain [38] is used to describe the lattice mismatch around the defects,

$$\varepsilon_{ij}^*(\mathbf{r}, t) = \varepsilon_0^{vac} c_{vac}(\mathbf{r}, t)\delta_{ij} + \varepsilon_{ij}^{gas}(c_{gas}(\mathbf{r}, t)) + \varepsilon_{ij}^{dis}(\eta_{lm}(\mathbf{r})) + \varepsilon_{ij}^{G.B}(\phi(\mathbf{r})), \quad (3)$$

where $\varepsilon_0^{vac} = (1/a)da/(dc_{vac})$ is the expansion coefficient of lattice parameters with respect to c_{vac}. Here, we assume that the variation of the stress-free lattice parameter, a, with vacancy concentration obeys Vegard's law and δ_{ij} is the Kronecker-Delta function. The eigenstrain tensor $\varepsilon_{ij}^{gas}(c_{gas}(\mathbf{r}, t))$ is associated with the lattice mismatch due to gas atoms. It is calculated by $\varepsilon_{ij}^{gas}(c_{gas}(\mathbf{r}, t)) = \varepsilon_0^{gas} c_{gas}(\mathbf{r}, t)\delta_{ij}$ in the matrix, and $\varepsilon_{ij}^{gas}(c_{gas}(\mathbf{r}, t)) = P(c_{gas}(\mathbf{r}, t))/(3B)\delta_{ij}$ in the gas phase, where $P(c_{gas}(\mathbf{r}, t))$ is the relationship between concentration and pressure in the gas phase, and B is the bulk modulus of the gas phase. The third term is the eigenstrain related to a spatial distribution of dislocations, which can be written as [28,30]:

$$\varepsilon_{ij}^{dis}(\mathbf{r}) = \sum_{l,m} \frac{1}{2d_0^{lm}} [b_i^{lm} n_j^{lm} + b_j^{lm} n_i^{lm}] \eta_{lm}(\mathbf{r}), \quad (4)$$

where b^{lm}, n^{lm} and d_0^{lm} are the Burgers' vector, the normal of the slip plane, and the interplanar distance of the slip plane, respectively. The lattice distortion along grain boundaries can be described by dislocation and vacancy distributions, so the last term $\varepsilon_{ij}^{G.B.}(\phi(\mathbf{r}))$ is calculated in the same manner as the first and third terms.

The mechanical equilibrium equations are written as:

$$\frac{\partial \sigma_{ij}}{\partial r_j} = \frac{\partial \lambda_{ijkl} e_{kl}}{\partial r_j} = 0, \quad (5)$$

where e_{kl} is the elastic strain component, which can be obtained by subtracting the eigenstrain ε_{kl} from the total strain ε_{kl}, i.e., $e_{kl} = \varepsilon_{kl} - \varepsilon_{kl}^*$, and λ_{ijkl} is the elastic stiffness tensor. In this work, the elastic stiffness is assumed to be inhomogeneous and is expressed as a statistical average of the stiffness of the matrix:

$$\lambda_{ijkl} = \lambda_{ijkl}^0(1 - c_{vac}(\mathbf{r}, t)) + \lambda_{ijkl}' c_{gas}(\mathbf{r}, t). \quad (6)$$

This expression ensures that elastic constants are zero in voids where c_{vac} = 1 and c_{gas} = 0. In gas bubbles c_{vac} = 1 and $c_{gas} \neq 0$ the elastic constants depend on the gas concentration. Specifically, we do not treat the gas bubbles as a solid phase, which may be more accurate at high gas pressures. The mechanical equilibrium equations are solved by an iteration method proposed in Refs. [27,39]. Then the elastic energy is calculated by:

$$F^{elastic} = \frac{1}{2}\lambda_{ijkl} e_{ij} e_{kl}. \quad (7)$$

2.3. Evolution equations

The migration of vacancies and gas atoms is described by the Cahn–Hilliard equations [40]:

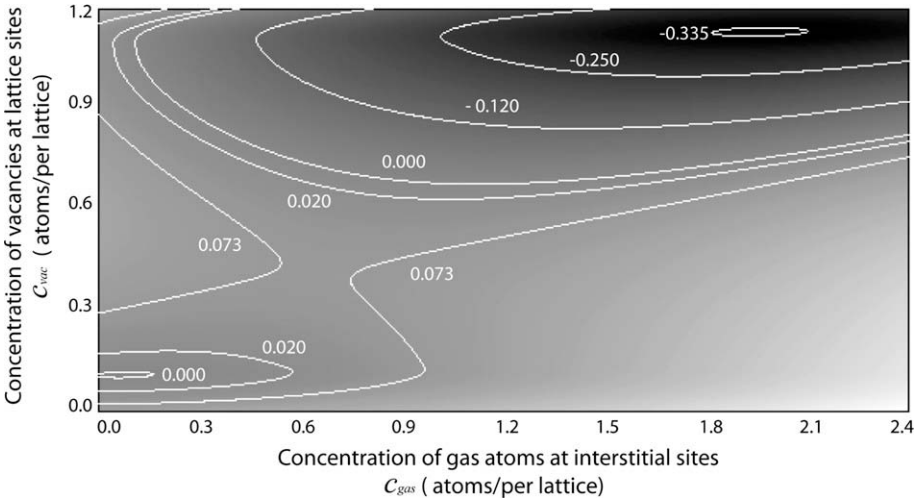

Fig. 1. Chemical free energy F/C_{44} as a function of He gas concentration and vacancy concentration in the unit of atom/lattice site, which provides solid solution and gas bubble phase equilibrium. C_{44} (GPa) is the shear modulus of the matrix.

Table 1
The dimensionless parameters used in the simulations.

Time	Δt^*	0.0005
Coefficient of chemical free energy	f^*_{gas}	0.100
Coefficient of chemical free energy	f^*_{vac}	1.102
Coefficient of chemical free energy	E^*	−0.2
Coefficient of chemical free energy	A	−1.663
Coefficient of chemical free energy	B	0.313
Coefficient of chemical free energy	C	0.357
Coefficient of chemical free energy	D	−0.012
Solubility of gas atoms (atom/lattice site)	c^0_{gas}	0.012
Solubility of vacancies (atom/lattice site)	c^0_{vac}	0.032
Gradient coefficient	κ^*_{gas}	0.06
Gradient coefficient	κ^*_{vac}	0.06
Elastic constants of matrix	λ^0_{ijkl}/C_{44}	$C_{11}/C_{44} = 3$; $C_{12}/C_{44} = 1$; $C_{44}/C_{44} = 1$
Elastic constants of gas bubbles	λ^l_{ijkl}/C_{44}	$C'_{11}/C_{44} = 5/3$; $C'_{12}/C_{44} = 5/3$; $C'_{44}/C_{44} = 0$

$$\frac{\partial c_{gas}(\mathbf{r},t)}{\partial t} = \nabla \cdot M_{gas} \nabla \frac{\delta E(c_{gas}, c_{vac})}{\delta c_{gas}(\mathbf{r},t)} + \dot{g}_{gas}(\mathbf{r},t), \tag{8}$$

$$\frac{\partial c_{vac}(\mathbf{r},t)}{\partial t} = \nabla \cdot M_{vac} \nabla \frac{\delta E(c_{gas}, c_{vac})}{\delta c_{vac}(\mathbf{r},t)} + \dot{g}_{vac}(\mathbf{r},t), \tag{9}$$

where $E(c_{gas}, c_{vac})$ is the total free energy described by Eq. (1) and $\dot{g}_{gas}$ and $\dot{g}_{vac}$ are generation rates of gas atoms and vacancies, respectively. They are simply described as a linear function of vacancy concentration $\dot{g}_i(\mathbf{r},t) = \dot{g}^0_i(1 - c_{vac}(\mathbf{r},t))$, $(i = gas, vac)$ so that the generation rates are zero in both voids and gas bubbles. Here, we note that the sinks for point defects are naturally introduced by adding structural defects such as vacancy clusters, dislocations, and grain boundaries in our simulations and allowing vacancies to be absorbed at these sites. M_{gas} and M_{vac} are the mobility of gas atoms and vacancies, respectively, noting that the mobility of point defects is usually very different in grains, grain boundaries, and voids, and depends strongly on composition and temperature. In this work, the mobility is described as $M_i = M^0_i\ (1 + 3(\exp(\phi) - 1)$, which gives mobility in grain boundaries and gas bubbles much larger than in grains.

The evolution Eqs. (8) and (9) are efficiently solved using a semi-implicit method [41], using dimensionless units:

$$r^*_i = \frac{r_i}{r_0}, \quad t^* = \frac{M^0_{gas} t}{r_0^2 C_{44}}, \quad f^*_{gas} = \frac{f_{gas}}{C_{44}}, \quad f^*_{vac} = \frac{f_{vac}}{C_{44}}, \quad E^* = \frac{E}{C_{44}}, \kappa^*_{gas} = \frac{\kappa_{gas}}{r_0^2 C_{44}}, \quad \kappa^*_{vac} = \frac{\kappa_{vac}}{r_0^2 C_{44}}, \quad \lambda^*_{ijkl} = \frac{\lambda_{ijkl}}{C_{44}}, \tag{10}$$

where r_0 is a characteristic length, and C_{44} is the shear modulus of the matrix. Table 1 lists all the model parameters used in the simulations.

3. Results and discussion

3.1. Formation and growth of gas bubbles around defects

Trapping of vacancies and gas atoms by defects is a possible formation mechanism of voids and gas bubbles. To examine this hypothesis, the segregation of vacancies and gas atoms around two defects was studied: a shear dislocation loop and a vacancy cluster, both of which are often observed in fuels and cladding materials. In the simulations, a square dislocation loop with $b = [1\,0\,\bar{1}]$, $n = [1\,1\,1]$ and an edge length $L_0 = 40r_0$; and a spherical vacancy cluster with average vacancy concentration $c_{vac} = 0.2$ and a radius $R_0 = 2r_0$ is put in the center of a simulation cell $128r_0 \times 128r_0 \times 128r_0$, respectively. The simulations start from a uniform vacancy concentration $c_{vac} = 0.03$ and gas concentration $c_{gas} = 0.03$. Although any concentration of vacancies and gas atoms can be used in our model, high concentrations are used in order to accelerate the simulation. The gas atom and vacancy generation rates are given by $\dot{g}^0_{gas} = \dot{g}^0_{vac} = 0.002(t^*)^{-1}$. The vacancy is assumed to cause a volume contraction while a gas atom results in a volume expansion, where $\varepsilon^{vac}_0 = -0.01$, $\varepsilon^{gas}_{ij}(c_{gas}(\mathbf{r},t)) = 0.015 c_{gas}(\mathbf{r},t)\delta_{ij}$ in the matrix, and $\varepsilon^{gas}_{ij} = P(c_{gas}(\mathbf{r},t))/(3B)\delta_{ij}$ in gas bubbles are used in Eq. (3). $P(c_{gas}(\mathbf{r},t))$ is the pressure–concentration relation of the He gas phase [17,36,37]. The bulk modulus B of the He gas phase is assumed to be the same as the matrix. It is true that the gas bulk modulus depends on the concentration. But if the pressure–concentration relationship is used to calculate the eigenstrain, the bulk modulus is just a scale factor, and does not affect the resulting pressure in the gas phase. The shear modulus of the He gas phase is assumed to be zero in the simulations although the He gas phase may become a solid phase under a high pressure. It needs to be pointed out that this model allows inhomogeneity and anisotropy of both the matrix and gas phases. The temporal evolution of the vacancy and He concentration profiles around the dislocation loop are plotted in Fig. 2. As expected, He atoms initially segregate in the tensile region of the edge dislocation while vacancies locate in the compressive region of the edge dislocation. There is no segregation observed on the screw dislocation segments because the hydrostatic stress around a screw dislocation is zero. With the increase of overall He and vacancy concentrations, more and more He and vacancies segregate near dislocations, and then vacancies in the compressive region of the dislocation start to diffuse and combine with He atoms; finally a gas bubble forms in the tensile region of the dislocation.

The combination of segregated vacancies and He atoms leads to gas bubble formation. Either vacancies diffusing to gas atoms or gas atoms diffusing to vacancies is possible, but which process dominates depends on the mobility of defects and driving forces associated with the minimization of the chemical free energy and the elastic energy. It is interesting to find that gas atoms diffusing to vacancies occurs when decreasing the lattice mismatch strains of gas atoms and increasing the lattice mismatch strain due to vacancies. Fig. 3 shows the temporal evolution of the vacancy and gas concentration profiles. Comparing Figs. 2 and 3, we can see that the gas bubble may form in either tensile or compressive regions of the dislocation depending on the lattice mismatch strains of the vacancy and gas atom. The results imply that accurate formation volume of defects, which is used to calculate the lattice mismatch strains, is required for quantitative simulations.

The temporal evolution of the vacancy and gas concentration around a vacancy cluster with an initial vacancy concentration 0.2 is shown in Fig. 4. The concentration isosurface shows a profile where the concentration is 95% of the maximum concentration. Therefore, the isosurface presents the temporal evolution of the maximum concentration as well as the size of the gas cluster or

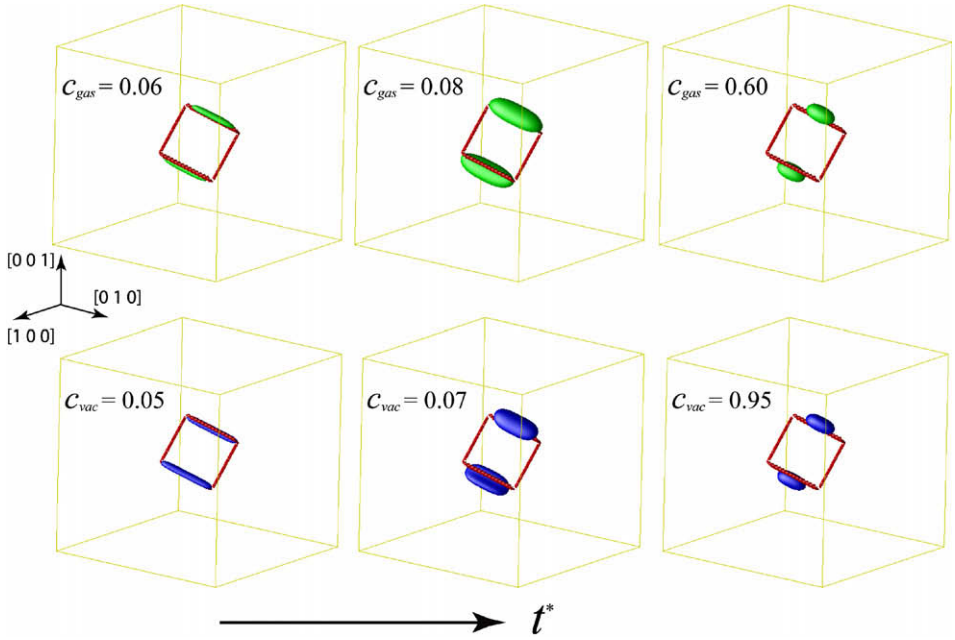

Fig. 2. Temporal evolution of He and vacancy concentration profiles around a square dislocation loop with $b = [1\,0\,\bar{1}]$, $n = [1\,1\,1]$ and edge length $L_0 = 40r_0$. $\varepsilon_0^{gas} = 0.015$, $\varepsilon_0^{vac} = -0.01$ are used. Top row presents He concentration while bottom row gives vacancy concentration. The concentration isosurface shows a profile where the concentration is 95% of the maximum concentration.

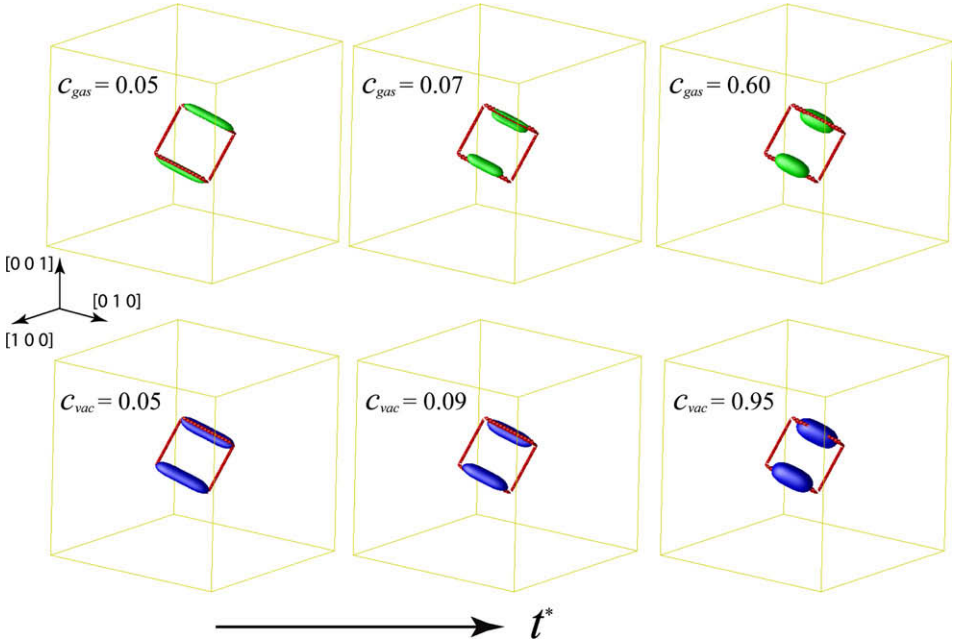

Fig. 3. Temporal evolution of He and vacancy concentration profiles around a square dislocation loop with $b = t[1\,0\,\bar{1}]$, $n = [1\,1\,1]$ and edge length $L_0 = 40r_0$. $\varepsilon_0^{gas} = 0.01$, $\varepsilon_0^{vac} = -0.015$ are used. Top row gives He concentration and bottom row the vacancy concentration. The concentration isosurface shows a profile where the concentration is 95% of the maximum concentration.

bubble. We can see that at early stages the concentration of the vacancy cluster decreases and the vacancy cluster shrinks because the vacancy cluster is unstable. But the gas concentration at a vacancy cluster increases gradually due to the elastic interaction (a combination of gas atoms and vacancies reduces the elastic energy) and chemical interaction (a combination of gas atoms and vacancies reduces the chemical free energy). The increasing segregation of gas atoms at vacancy clusters finally stabilizes the vacancy cluster and leads to the gas bubble formation and growth. Whether or not an initial vacancy cluster can act as a formation site for a gas bubble depends on the vacancy cluster size as well as the kinetics of vacancies and gas atoms, i.e., their mobility and generation rates.

3.2. Growth kinetics of a single gas bubble around a vacancy cluster

The formation and growth of gas bubbles require a supply of vacancies and He atoms. The effect of vacancy generation rate

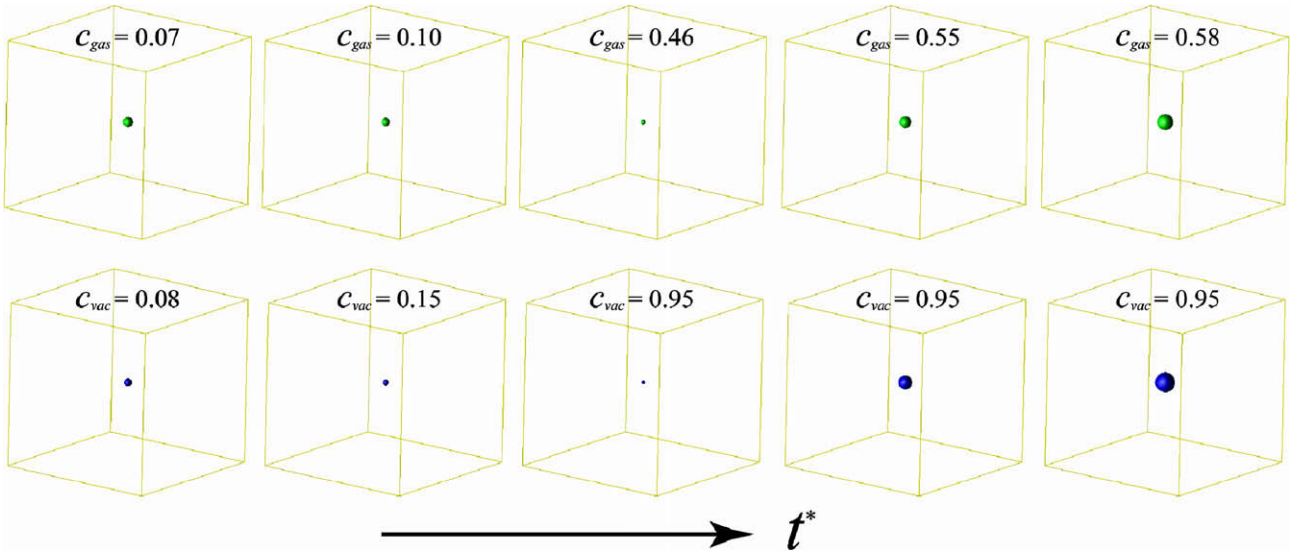

Fig. 4. Temporal evolution of He and vacancy concentration profiles around a spherical vacancy cluster with average vacancy concentration $c_{vac} = 0.2$ and radius $R_0 = 2r_0$. $\varepsilon_0^{gas} = 0.015$, $\varepsilon_0^{vac} = -0.01$ are used. Top row presents He concentration while bottom row is vacancy concentration.

and mobility on the gas bubble nucleation and growth kinetics was studied by simulating the evolution of a vacancy cluster with different vacancy generation rates and mobility. The initial vacancy cluster is a sphere with average vacancy concentration $c_{vac} = 0.2$ and a radius $R_0 = 2r_0$. The gas bubble diameter can be calculated by assuming that the vacancy concentration in the gas bubble is larger than 0.95. Fig. 5 presents the evolution of gas bubble diameters. These results show that (1) if the vacancy generation rate is zero, the initial vacancy cluster decays as shown by the black-circle line; (2) if the vacancy generation rate is not zero, gas bubble formation and growth takes place. This shows that the vacancy mobility has different effects on the bubble formation and growth. Bubble formation increases as the vacancy mobility decreases. In contrast, the gas bubble growth rate (dr_0/dt^*) decreases with the decrease of the vacancy mobility.

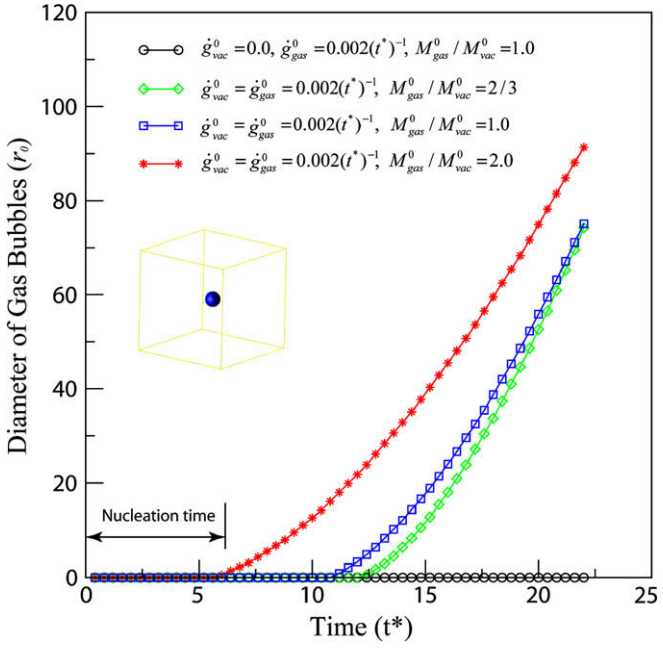

Fig. 5. Effect of vacancy mobility and generation rate on gas bubble nucleation and growth at a vacancy cluster. t^* is a reduced time defined in Eq. (10).

3.3. Gas bubble evolution in a polycrystalline material

The simulations discussed above were done in three dimensions. The size of the simulation cell is limited by computer resources. In order to examine the effect of a grain boundary on gas bubble evolution, two-dimensional simulations were performed with a larger simulation cell, $1024r_0 \times 1024r_0$. A polycrystal was generated by applying a grain growth phase-field model [42]. Grain boundaries in a polycrystalline material are two-dimensional defects which usually have free volume (more open atom structure compared to perfect crystals) especially for large angle grain boundaries. As a result, the mobility of atoms and vacancies are considerably different along grain boundaries and inside grains. For instance, MD simulations show that the migration energy (Em) for a vacancy in the Fe matrix is about 0.7 eV and about 0.4 eV in the grain boundaries examined. Interstitial He atoms are extremely mobile in the Fe perfect crystal (Em = 0.1 eV) and can become trapped in the excess volume of the grain boundary where they have Em = 0.4 eV [43].

In order to take the grain boundary features into account in the simulations, randomly distributed immobile vacancies are used to describe the free volume. The lattice mismatch associated with the free volume in the grain boundaries is described by stress free strains $\varepsilon_{ij}^{G.B.}(\phi(\mathbf{r})) = 0.033\sin(\phi(\mathbf{r})\pi/2)\delta_{ij}$. The mobility of vacancies and gas atoms in the grain boundaries is assumed to be five times larger than in grains. Hundred small vacancy clusters with a radius varying $1/3r_0$ and average vacancy concentration of 0.2 are randomly distributed in the simulation cell; the overall initial concentration of vacancies and gas atoms are 0.03; and the generation rates are $\dot{g}^0_{gas} = \dot{g}^0_{vac} = 0.003(t^*)^{-1}$. The grain boundaries and vacancy clusters are sinks to both gas atoms and vacancies. The time evolution of the gas bubbles is shown in Fig. 6. The color bar presents the gas atom concentration, which varies from 0 to 1.32 and the purple lines show the grain boundaries. This shows that gas atoms first segregate on the grain boundaries and vacancy clusters due to local tensile stress fields associated with the free volume. Then, gas bubbles form, grow or shrink, and coalesce because of relative large mobility in grain boundaries. The gas bub-

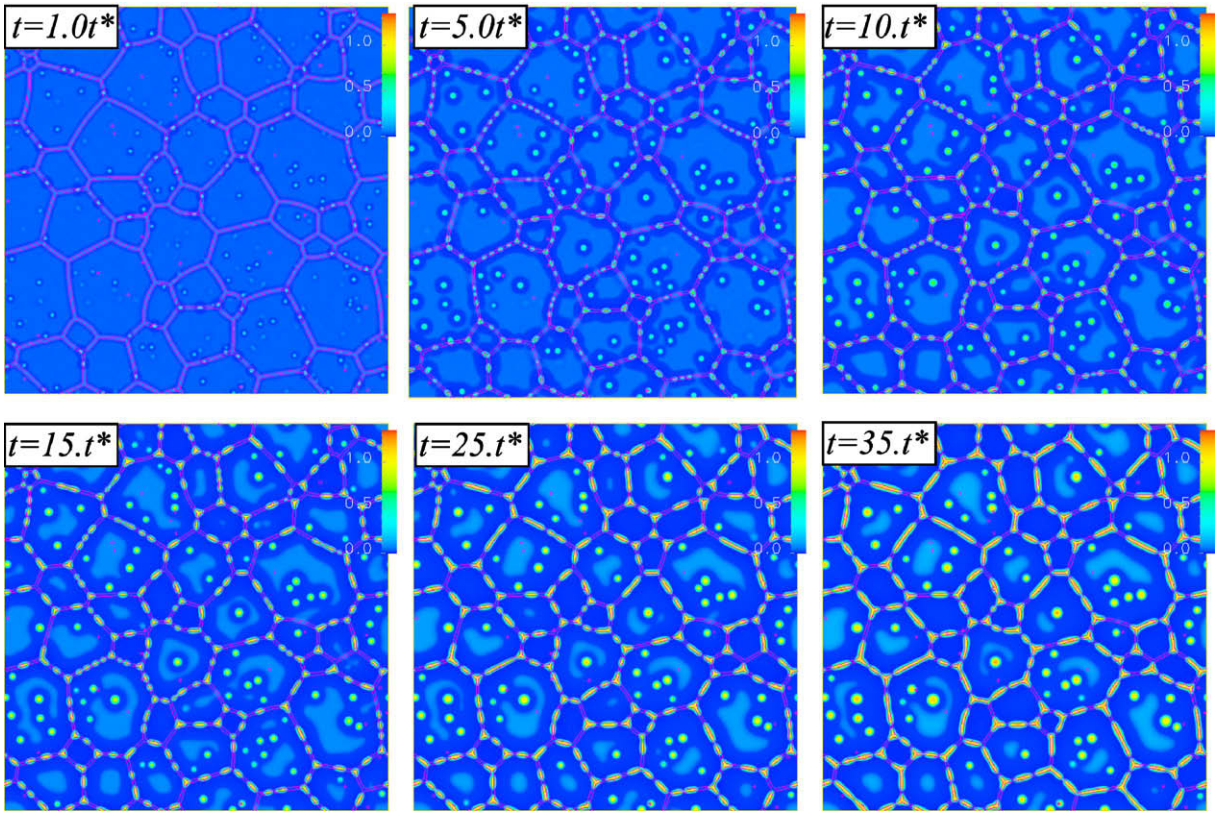

Fig. 6. Time evolution of gas bubbles in a polycrystalline material. The color bar presents the He concentration which varies from 0 to 1.32. The purple lines show the grain boundaries. (For interpretation of the references in colour in this figure legend, the reader is referred to the web version of this article.)

ble formation in the grain boundaries consumes the vacancies and gas atoms around the grain boundaries. As a result, gas bubbles rarely form near grain boundaries; the newly formed vacancy plus gas atom clusters vanish because not enough vacancies and gas atoms are available, and a gas bubble free zone, so called denuded zone, forms around the grain boundaries as observed in experiments [4]. The effect of vacancy mobility and generation rate on the gas bubble formation was also simulated and showed that lower vacancy mobility and/or higher vacancy generation rates may cause the formation of intragranular gas bubbles.

3.4. Effective thermal conductivity

Point defects [44], second phase such as voids and gas bubbles, grain-boundaries [45], and stress fields [46] all may affect the local thermal conductivity. Phase-field simulations output the temporal evolution of point defect distributions, gas bubble and void microstructures as well as the stress fields and this information can be used to calculate the local thermal conductivity $K(\mathbf{r},T)$. For a given microstructure, the effective thermal conductivity can be calculated using the following scheme. The heat transport equation,

$$\frac{\partial T}{\partial t} = \nabla \cdot K(\mathbf{r},T)\nabla T, \tag{11}$$

under constant temperature boundary conditions can be solved along the r_1 axis, i.e., $T = T_1|_{r_1=0}$ and $T = T_2|_{r_1=L}$ where T is the temperature. When the temperature reaches a steady state, the effective thermal conductivity is calculated by:

$$\overline{K} = \frac{\bar{J}_Q}{\langle \partial T/\partial r_1 \rangle} \tag{12}$$

where $\bar{J}_Q$ is the average heat flux, and $\langle \partial T/\partial r_1 \rangle$ is the average temperature gradient. Studying the coupling between heat transport and defect migration, requires considering the temperature dependence of thermodynamic and kinetic properties, and simultaneously solving Eqs. (8), (9) and (11). The temperature dependence of the thermal conductivity and the mobility of vacancies and gas atoms is ignored. Therefore, the gas bubble evolution

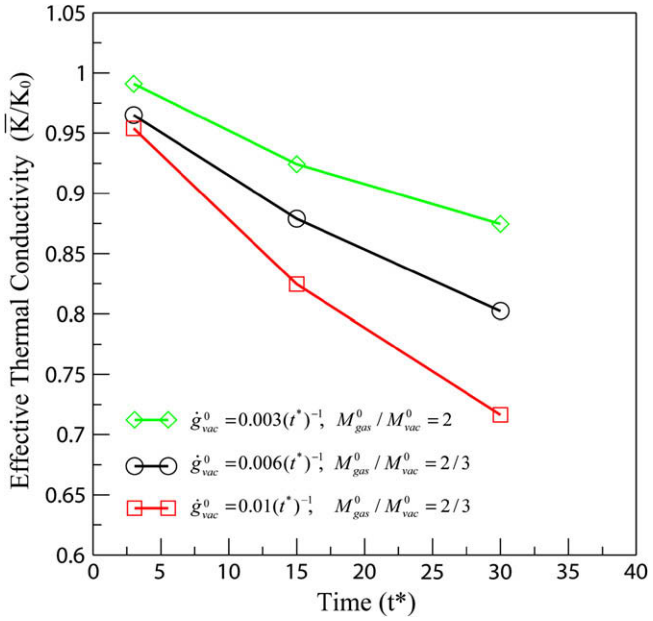

Fig. 7. Evolution of effective thermal conductivity under three material processes with different vacancy mobility and vacancy generation rates. t^* is a reduced time defined in Eq. (10).

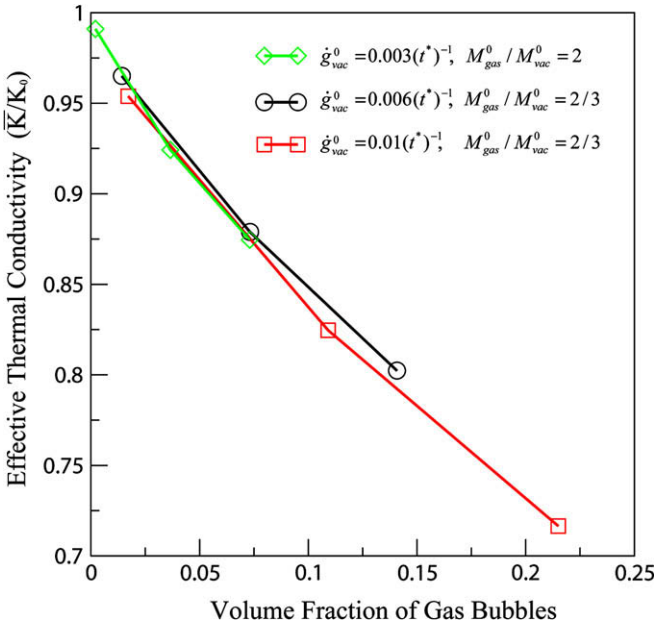

Fig. 8. Dependence of effective thermal conductivity on the gas bubble volume fraction.

Eqs. (8) and (9) and the temperature evolution Eq. (11), are solved separately. In the simulations, the thermal conductivity is assumed to be a function of the vacancy concentration as $K(\mathbf{r})/K_0 = 1 - 0.8\sin(c_{vac}(\mathbf{r})\pi/2)$, which gives the thermal conductivity in gas bubbles ($c_{vac}(\mathbf{r}) \approx 1.0$) being about five times smaller than that in the matrix ($c_{vac}(\mathbf{r}) \approx 0.0$).

Systematic simulations, including the effect of grain boundaries, gas bubbles, point defects and stresses on the effective thermal conductivity, are under way. Fig. 7 shows the evolution of effective thermal conductivity calculated under three material processes with different vacancy mobility and vacancy generation rates. This shows that the effective thermal conductivity depends strongly on both the vacancy mobility and generation rate. Lower vacancy mobility and generation rate lead to a slower decrease of the effective thermal conductivity because of a slower gas bubble growth rate. For the same vacancy mobility, a higher vacancy generation rate results in a faster gas bubble growth. As a consequence, the effective thermal conductivity decreases faster. Fig. 8 shows the dependence of effective thermal conductivity on gas bubble volume fraction. The results demonstrate that gas bubble volume fraction is the main determinant to the effective thermal conductivity while the effective thermal conductivity is not sensitive to the gas bubble morphology, which is the expected result.

4. Conclusions

This work presented a phase-field approach to modeling the gas bubble evolution and calculating the effective thermal conductivity in a polycrystalline material with the microstructure obtained from the simulations. The dependence of bubble formation and growth kinetics on small vacancy clusters, dislocations and grain boundaries, the generation rates and mobility of fission products, and the evolution of effective thermal conductivity have been simulated. The results show that the gas bubble nucleation at grain boundaries is much easier than inside grains because of the free volume trapping of gas atoms and faster supplement of vacancies and gas atoms. Helium bubble formation around an unstable vacancy cluster generated by irradiation depends on the vacancy mobility and the further supply of vacancies and He. The formation volume of the vacancy and He has a strong effect on the gas bubble nucleation on dislocations. The simulations also show that the effective thermal conductivity is strongly influenced by the bubble volume fraction and less influenced by the morphology of the bubbles. Although the results are qualitative, these simulations confirm that the phase-field approach is a promising and predictable computational tool for quantitatively studying and predicting phase stability, microstructure and property evolution in nuclear materials in a severe radiation environment. Reliable predictions will follow the development of accurate thermodynamic and kinetic properties of the system. The models developed in this work can be extended to study different material phenomena observed in nuclear fuels and cladding materials, including grain growth, bubble formation and evolution, oxidation, hydrogen embrittlement, and the coupling of these processes. In the present phase-field model, the expressions of thermodynamic and kinetic data are given in very general forms that can be replaced with specific thermodynamic and kinetic data appropriate for quantitative simulations.

Acknowledgments

This work was supported at Pacific Northwest National Laboratory and Los Alamos National Laboratory by the US Department of Energy. PNNL is operated for the US Department of Energy by Battelle Memorial Institute under Contract DE-AC06-76RLO 1830. S.Y. Hu wants to thank Dr Ken Geelhood and Dr Rick Kurtz at PNNL and Dr Xiang-Yang Liu at LANL for their helpful discussions.

References

[1] Roger E. Stoller, J. Nucl. Mater. 174 (1990) 289.
[2] H. Stehle, J. Nucl. Mater. 153 (1988) 3.
[3] I. Zacharie, S. Lansiart, P. Combette, M. Trotabas, M. Coster, M. Groos, J. Nucl. Mater. 255 (1998) 85.
[4] I. Zacharie, S. Lansiart, P. Combette, M. Trotabas, M. Coster, M. Groos, J. Nucl. Mater. 255 (1998) 92.
[5] T. Sonoda, M. Kinoshita, I.L.F. Ray, T. Wiss, H. Thiele, D. Pellottiero, V.V. Rondinella, H.J. Matzke, Nucl. Instrum. and Meth. B 191 (2002) 622.
[6] R.C. Birtcher, S.E. Donnelly, C. Templier, Phys. Rev. B50 (1994) 764.
[7] G. Sattonnay, F. Garrido, L. Thome, Philos. Mag. 84 (2004) 109.
[8] C.T. Walker, W. Goll, T. Matsumura, J. Nucl. Mater. 245 (1997) 169.
[9] C. Hobson, R. Taylor, J.B. Ainscough, J. Phys. D: Appl. Phys. 7 (1974) 1003.
[10] I. Monnet, P. Dubuisson, Y. Serruys, M.O. Ruault, O. Kaitasov, B. Jouffrey, J. Nucl. Mater. 335 (2004) 311.
[11] R.G. Pahl, C.E. Lahm, S.L. Hayes, J. Nucl. Mater. 204 (1993) 141.
[12] C.C. Dollins, J. Nucl. Mater. 59 (1975) 61.
[13] M.H. Yoo, J. Nucl. Mater. 68 (1977) 193.
[14] M.S. Veshchunov, J. Nucl. Mater. 277 (2000) 67.
[15] N.M. Ghonium, S. Sharafat, J.M. Williams, L.K. Mansur, J. Nucl. Mater. 117 (1983) 96.
[16] S. Sharafat, N.M. Ghoniem, J. Nucl. Mater. 283–287 (2000) 789.
[17] K. Morishita, R. Sugano, J. Nucl. Mater. 353 (2006) 52.
[18] J. Rest, S.A. Zawadzki, A Mechanistic Model for the Prediction of Xe, I, Cs, Te, Ba and Sr Release from Nuclear Fuel under Normal and Severe-Accident Conditions, NUREG/CR-5840 TI92 040783, 1994.
[19] T.J. Heames, D.A. Williams, N.E. Bixler, A.J. Grimley, C.J. Wheatley, N.A. Johns, P. Domagala, L.W. Dickson, C.A. Alexander, I. Osborn-Lee, S. Zawadzki, J. Rest, A. Mason, R.Y. Lee, VICTORIA: A Mechanistic Model of Radionuclide Behavior in the Reactor Coolant System under Severe Accident Conditions, NUREG/CR-5545, 1992.
[20] M.S. Veshchunov, V.D. Ozrin, V.E. Shestak, V.I. Tarasov, R. Dubourg, G. Nicaise, Nucl. Eng. Des. 236 (2006) 179.
[21] M.S. Veshchunov, R. Dubourg, V.D. Ozrin, V.E. Shestak, V.I. Tarasov, J. Nucl. Mater. 362 (2007) 327.
[22] G.A. Berna, C.E. Beyer, K.L. Davis, D.D. Lanning, FRAPCON-3: A Computer Code for the Calculation of Steady-State, Thermal Mechanical Behavior of Oxide Fuel Rods for High Burnup, NUREG/CR-6534, vol. 2 (PNNL-11513 v.2, Pacific Northwest National Laboratory, Richland, WA), 1997.
[23] L.Q. Chen, Ann. Rev. Mater. Res. 32 (2002) 113.
[24] A. Karma, W.J. Rappel, Phys. Rev. E57 (1998) 4323.
[25] Y.L. Li, S.Y. Hu, Z.K. Liu, L.Q. Chen, Appl. Phys. Lett. 81 (2002) 427.
[26] Y. Wang, L.Q. Chen, A.G. Khachaturyan, Scr. Metall. 25 (1991) 1387.
[27] S.Y. Hu, L.Q. Chen, Acta Mater. 49 (2001) 1879.
[28] Y.U. Wang, Y.M. Jin, A.M. Cuitino, A.G. Khachaturyan, Appl. Phys. Lett. 78 (2001) 2324.

[29] D. Rodney, Y. Le Bouar, A. Finel, Acta Mater. 51 (2003) 17.
[30] S.Y. Hu, Y.L. Li, Y.X. Zheng, L.Q. Chen, Int. J. Plasticity 20 (2004) 403.
[31] J.E. Guyer, W.J. Boettinger, J.A. Warren, Phys. Rev. E69 (2004) 21603.
[32] W.D. Wilson, C.L. Bisson, M.I. Baskes, Phys. Rev. B15 (1981) 5616.
[33] A.J. Schwartz, W.G. Wolfer, J. Comput.-Aided Mater. Des. 14 (2007) 331.
[34] T. Suzudo, H. Kaburaki, M. Itakura, E. Wakai, Model. Simul. Mater. Sci. Eng. 16 (2008) 1.
[35] L.L. Bonilla, A. Carpio, J.C. Neu, W.G. Wolfer, Physica D222 (2006) 131.
[36] R.L. Mills, D.H. Liebenberg, J.C. Bronson, Phys. Rev. B21 (1980) 5137.
[37] H. Trinkaus, Radiat. Eff. Defect Solids 78 (1983) 189.
[38] J.D. Eshelby, Proc. Roy. Soc. A241 (1957) 376.
[39] A.G. Khachaturyan, Theory of Structural Transformations in Solids, Wiley, New York, 1983.
[40] J.W. Cahn, Acta Metall. 9 (1961) 795.
[41] L.Q. Chen, J. Shen, Comput. Phys. Comm. 108 (1998) 147.
[42] C.E. Krill, L.Q. Chen, Acta Mater. 50 (2002) 3957.
[43] F. Gao, H.L. Heinisch, R.J. Kurtz, J. Nucl. Mater., in press.
[44] P.G. Klemens, Phys. Rev. 119 (1960) 507.
[45] H.B.G. Casimir, Physica (Utrecht) 5 (1938) 495.
[46] W.H. Tang, J. Phys. Chem. Solids 62 (2001) 1943.